

pubs.acs.org/JPCC Article

Chemical and Valence Electron Structure of the Core and Shell of Sn(II)-Perovskite Oxide Nanoshells

Gowri Krishnan, Shaun O'Donnell, Rachel Broughton, Jacob L. Jones, D. J. Osborn, Thomas D. Small, Theresa Block, Aylin Koldemir, Rainer Pöttgen, Gregory F. Metha, Paul A. Maggard, and Gunther G. Andersson*



Cite This: J. Phys. Chem. C 2024, 128, 17387-17398



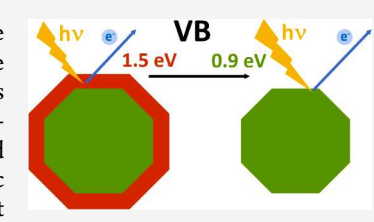
ACCESS

III Metrics & More

Article Recommendations

s Supporting Information

ABSTRACT: Photocatalytic reactions occur at surfaces; therefore, understanding the valence electronic structure of a photocatalyst is an important aspect in the selection of suitable materials. A new class of kinetically stable metastable Sn(II)-perovskite oxide nanoshell was synthesized previously, which has a core—shell (BZT-SZT) ((Ba($Zr_{1-y}Ti_y$)O $_3$ -Sn($Zr_{1-y}Ti_y$)-O $_3$)) structure, but the electronic structure was not fully resolved. This work reports a detailed electron spectroscopic study of BZT-SZT (or BSZT) to determine the valence electronic structure and the chemical nature of the surface near region with a focus on Sn as the element added to the outer shell via a molten-salt reaction. Near edge X-ray absorption fine structure was



used to understand the chemical state of Sn in the BSZT. X-ray photoelectron spectroscopy reveals that the flux reaction of Sn into the BZT does not significantly change the oxidation state of Sn, but the chemical environment of Sn changes from the surface to the bulk, and the chemical state of Sn corresponds to the Sn(II)-based oxide based on NEXAFS and ¹¹⁹Sn Mössbauer spectroscopy. The increase in Sn content decreases the valence band (VB) cutoff. The change in the VB occurs in the 2p O electron density region and is caused by the change in the Sn concentration. The change in the VB occurs to a stronger degree in the inner part of the BSZT and aligns with the change in the overall band gap from UV—vis measurements. Accordingly, it is likely that the condution band position at the surface does not depend on the amount of Sn content. The material developed is suitable for the oxidation half reaction of the overall water splitting reaction.

INTRODUCTION

Metal oxide semiconductors have been extensively used for the study and applications of photocatalytic reactions like water splitting. 1-4 TiO2 was initially the most widely used metal oxide for photocatalysis due to its low toxicity, stability in acidic and oxidative environments, and strong interaction with the metal support.⁵ An emerging class of photocatalyst materials is perovskites, which are cost-effective, abundant, and stable and have demonstrated good performance.⁶⁻⁸ Strontium titanate is a perovskite similar to titania and used for the photocatalytic reactions due to its chemical and structural stability, electronic structure tunability, and photocorrosion resistivity^{9,10} and a band gap similar to that of TiO_2 (~3.2 eV). Doping with various elements has been employed to reduce the band gap which improves the absorption of the solar spectrum toward its visible part; 11 however, this strategy has been only partially successful in reducing the band gap. The interest in small band gap materials has gained attention because of their ability to absorb light in the visible region of the solar spectrum, increasing their photocatalytic efficiency under solar radiation. For example, layered-perovskite metal oxides such as $A_5Nb_4O_{15}$ (A = Sr and Ba) have shown high activity for the water splitting reaction.¹²

Thermodynamically unstable metastable oxides have gained attention because of their ability to demonstrate distinct

physical, chemical, and electronic structure properties, which could be useful for photocatalytic water splitting. However, the synthesis of these materials is challenging. The Maggard and Jones groups have recently synthesized a new class of metastable oxides BZT-SZT $(Ba(Zr_{1-\nu}Ti_{\nu})O_3-Sn(Zr_{1-\nu}Ti_{\nu})-$ O₃) (BSZT) by a low-temperature flux reaction technique and form BSZT core-shell particles as the result of Sn(II) cation exchange. The high concentration of Sn(II) in the outer shell leads to a decrease in the band gap in this region of the material. 13,14 This class of materials was developed to help overcome the current challenges in the field of photocatalysis, which is the lack of absorption of light in the visible part of the solar spectrum. In the exchange reaction of SnClF with BZT, Sn exchanges with Ba forming BaClF and a shell of Sn-rich material SZT. Powder diffraction could be fitted best with a core of BZT and a shell of SZT plus a thin shell where Sn is partially oxidized. However, it remained unclear what the surface chemistry is and how the valence electron structure of

Received: June 23, 2024
Revised: September 12, 2024
Accepted: September 13, 2024
Published: October 2, 2024





the BSZT core, interface, and surface is different to that of the bulk after the Sn exchange reaction. 14

Due to the core/shell structure, it is of interest to understand the electronic structure of the core and the shell and how it is different from the bulk electronic structure. Furthermore, BSZT is of particular interest for photocatalysis, because the catalytic reaction occurs at the surface of the material. While this class of materials is metastable, it maintains its structure because the activation energy is high enough to inhibit phase segregation to more stable oxides under the reaction conditions. ^{13,14}

The aim of the present study is to understand how the incorporation of Sn(II) into the particles changes the surface chemistry of the BZT shell and its valence electron structure. For the material to be active as a photocatalyst for water splitting, the VB must be lower than the oxygen evolution and the conduction band (CB) must be higher than the hydrogen evolution reaction level. The valence electronic structure was studied by using VB X-ray photoelectron spectroscopy (VB-XPS) and the chemical structure by using X-ray photoelectron spectroscopy (XPS). Analyzing the VB structure at the surface is important for understanding the photocatalytic performance of the materials. Using VB-XPS allows the energy scale of the VB-XP spectra to be calibrated with the same method as for XPS. The same calibration method could not be applied to UPS because UPS and XPS cannot be measured simultaneously.¹⁹ Sn Mössbauer spectroscopy and near edge X-ray absorption fine structure (NEXAFS) are used to understand the chemical state of Sn in the sample.

EXPERIMENTAL METHODS

X-ray Photoelectron Spectroscopy (XPS). XPS is a surface-sensitive analytical technique used to analyze the chemical composition of the surface of the sample. XPS operates under high vacuum conditions. XPS uses soft X-rays as the source with a limited mean free path to excite electrons within the top 5-6 nm of the sample surface. The Mg K α line is used as the X-ray source with an excitation energy of 1253.6 eV. The emitted electron enters the hemispherical analyzer which measures the kinetic energy of the emitted electrons. X-ray photoelectron spectroscopy is surface-sensitive because of the limited electron mean free path of electrons in condensed matter, which is in the order of a few nanometers. Thus, only the top 1-10 nm of a sample contribute to an XP spectrum. The surface sensitivity can be quantified by

$$I(d, E, \alpha) = I_0 \exp\left(-\frac{d}{\cos(\alpha)}\lambda(E)\right)$$
(1)

where I_0 is the non-attenuated intensity, I is the intensity of the emitted electrons, d is the depth, α is the angle between the direction to the detector and the surface normal, and $\lambda(E)$ is the electron mean free path depending on the kinetic energy E of the electrons. As can be seen in (1), the surface sensitivity at a given angle of observation is determined by the electron mean free path. This parameter depends on the energy of the electrons and the composition of the sample 14 and is approximately 2–3 nm for the conditions used in the present work

The Auger parameter method is a powerful tool used to identify the chemical components rather than using photoelectron chemical shifts alone. The Auger parameter is defined as the difference in the binding energy between the photoelectron and the Auger line and is given by

$$\alpha = KE_A - KE_p = BE_A - BE_p \tag{2}$$

The kinetic energy is given by

$$BE = h\nu - KE \tag{3}$$

where KE_A and KE_p are the kinetic energy of an electron emitted form a specific element via an Auger process and a photoemission process, respectively.

The binding energy of all XP spectra was calibrated to 458.8 eV for Ti of ${\rm TiO_2}$ based on the average of the overall binding energy reported for ${\rm TiO_2}$ by NIST. The implications of this calibration are discussed throughout the manuscript. With this calibration, the O peak positions did not vary between samples; similarly, the Zr peak positions also did not change (with the exception of the Sn 0% sample as discussed below, which indicates that referencing to the ${\rm TiO_2}$ position is reliable).

For evaluating the VB-XPS data, the α_3 and α_4 satellites were taken into account by subtracting weighted spectra shifted by the respective energy. The contributions stemming from the satellites are not in the energy region for the VB cutoff and thus do not influence the determining of the VB cutoff positions. The VB cutoff is the main result derived from the VB-XPS data.

Near Edge X-ray Absorption Fine Structure (NEXAFS).

Near edge X-ray absorption fine structure (NEXAFS) is an Xray absorption spectroscopy technique used to determine the chemical state of the elements and their bonding environment. In NEXAFS, the sample is irradiated with soft X-rays, which results in photo absorption. The photo absorption process results in photoelectrons being emitted from the sample leaving holes behind in the core level. Subsequently the hole is either filled by an electron as a result of radiative emission of a fluorescent photon or by a non-radiative Auger electron. 16 The electrons emitted are detected, which results in an electron spectrum composed of Auger lines. These experiments were performed at the soft X-ray spectroscopy beamline at the Australian Synchrotron. The NEXAF spectra were detected using the emitted electrons, which makes the technique surface-sensitive. NEXAFS is used in the present work to determine the chemical state of SnO_x in the BZT sample, and the Quick AS NEXAFS Tool was used to extract the NEXAFS

Singular Value Decomposition (SVD) Algorithm. The SVD algorithm was applied for component analysis of the NEXAF spectra. The SVD follows two main steps: the first step is a mathematical procedure used to determine the number of individual base spectra required to fit the measured spectra. The base spectra obtained do not have to be physically meaningful. The number of base spectra is equal to the number of reference spectra. In the second step, a linear combination of the base spectra is used to determine the reference spectra. The two main criteria in determining the meaningful reference spectra are (i) that the reference spectra should be nonnegative and (ii) that the sum of the weighting factors used to fit the measured spectra with the reference spectra should be equal to unity.

¹¹⁹Sn Mössbauer Spectroscopy. A $Ca^{119m}SnO_3$ source was used for the Mössbauer spectroscopic experiments on SnO, SnO₂, and the quinary $(Ba_{0.8}Sn_{0.2})(Zr_{0.5}Ti_{0.5})O_3$ and $(Ba_{0.6}Sn_{0.4})(Zr_{0.5}Ti_{0.5})O_3$ samples. The measurements were

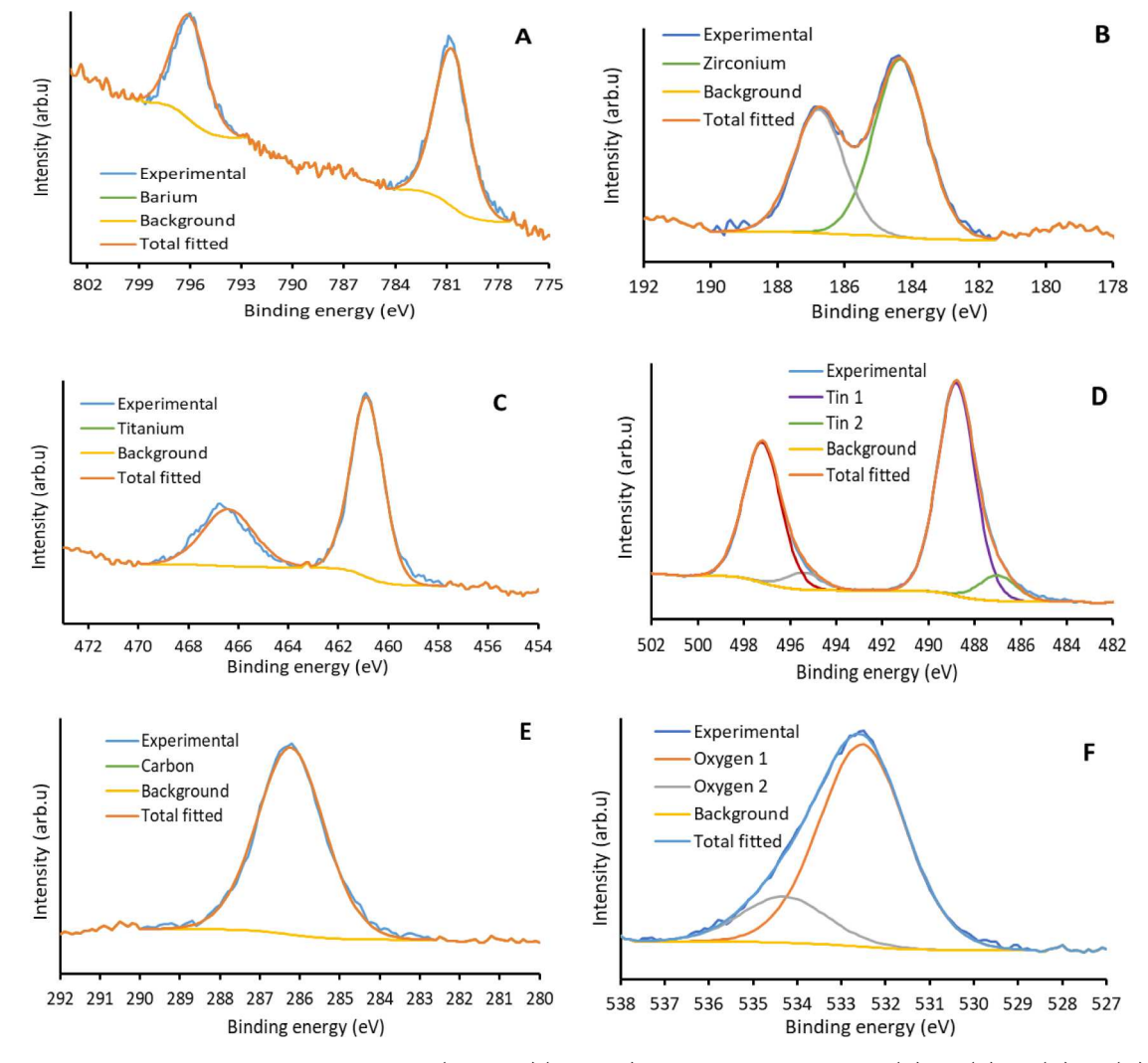


Figure 1. XPS fitting with the Shirley background for the $(Ba_{0.4}Sn_{0.6})(Zr_{0.5}Ti_{0.5})O_3$ sample after sputtering: (A) Ba, (B) Zr, (C) Ti, (D) Sn, (E) C, and (F) O.

carried out in a standard liquid nitrogen bath cryostat at 78 K. The source was kept at room temperature. The samples were mixed with alpha-quartz and enclosed in small PMMA containers at an optimized thickness. Fitting of the data was done by using the WinNormos for Igor6 program package. It should be noted that we discuss here the Mössbauer spectroscopic data published earlier and thus refer to these measurements.

Material and Sample Preparation. The BSZT- $((Ba_{1-x}Sn_x)(Zr_{1-y}Ti_y)O_3)$ samples (x=0-0.6, y=0.5) are prepared in powder form. The powder BSZT samples were uniformly spread on a vacuum compatible copper tape of 1×1 cm dimension. The samples were observed to charge during XPS analysis, which caused a shift of the spectra. An electron flood gun was used to compensate for the charging of the samples during the XPS analysis. The parameters of the flood gun were tuned such that the C peak position is close to 285 eV and the Ti $2p_{3/2}$ peak is close to 458.8 eV. The energy scale of the measured XP spectra was then calibrated with the Ti $2p_{3/2}$ peak to 458.8 eV as a reference position for the energy. The BSZT samples were sputtered with Ar⁺ at a kinetic energy of 3 keV to study the samples at a deeper layer and to compare with the structure at the surface. The sputtering dose used was 4×10^{15} ions/cm² over an area of ~ 1 cm² which roughly

sputters off 20 nm of the sample surface. In first instance, sputter depth profiling was used to remove the top part of the sample and to probe the deeper layers. The sputtering process could result in preferential sputtering of the light elements (e.g., O)²⁰ and thus potentially create a measurable fraction of reduced metal oxides. However, it was found that some of the metal oxides did not change their oxidation state when sputtering, and thus, it is assumed that this effect does not play a measurable role here. From our previous work, 19 the thickness of the outer shell of the nanoparticles subject to the Ba to Sn exchange reaction is up to 200 nm thick but could also have some thinner sections. The depth probed by XPS after sputtering is thus most likely mainly still in the outer shell but could also contain to some degree the inner core of the particles. The reason is that there is a variation in the thickness of the outer shell as can be seen in the EDS images in our previous work. 19

■ RESULTS AND DISCUSSION

XPS Results. The elements found in the XPS analysis of the $(Ba_{0.4}Sn_{0.6})(Zr_{0.5}Ti_{0.5})O_3$ sample are Ba, Zr, Ti, Sn, C, and O. High-resolution spectra recorded for these elements of the sputtered sample are shown in Figures 1A–F.

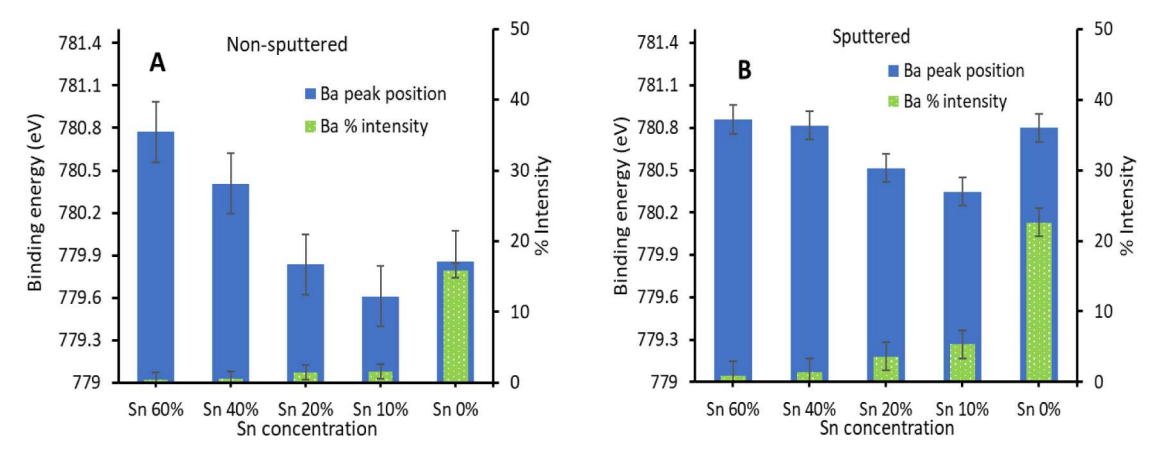


Figure 2. Plot of the binding energy vs % intensity of Ba: (A) nonsputtered and (B) sputtered.

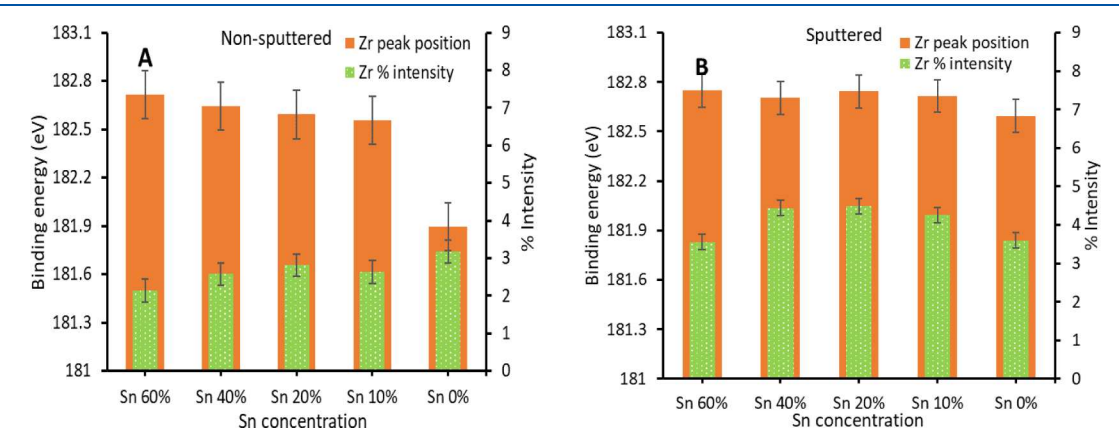


Figure 3. Plot of the binding energy vs % intensity of Zr: (A) nonsputtered and (B) sputtered.

The peak positions for Ba $3d_{5/2}$ of the nonsputtered samples for all samples with varying Sn content are shown in Figure 2A. The peak position of Ba $3d_{5/2}$ for the nonsputtered samples is found at a binding energy between 780.4 and 780.7 eV for samples with Sn concentrations of 40% and 60%. This binding energy is close to that of Ba compounds, with Ba being in a higher oxidation state and reduced electron density. The samples with lower Sn content (0%, 10%, and 20%) were found at a lower binding energy between 779.6 and 779.8 eV which is close to the binding energy found for BaO.²¹ It can be seen that the amount of Ba decreases with increasing concentrations of Sn and the Ba concentration of the 0% sample is significantly higher (about a factor of 10) than that of the Sn-containing samples. Overall, the increase in Sn content both shifts the binding energy of Ba toward a more highly oxidized state and decreases the density of Ba in the sample more than proporatinal to the increase in nominal Sn content.

The peak position of Ba $3d_{5/2}$ after sputtering is found at higher binding energies between 780.3 and 780.8 eV for the various Sn concentrations (0%, 10%, 20%, 40%, and 60%) which is close to that of BaO₂ at 780.5 eV.²² Similar to the nonsputtered samples, there is a decreasing trend in binding energy with decreasing Sn content. However, the changes in the binding energy are much smaller than for the nonsputtered sample and just outside the experimental uncertainty. Thus, the peak position of Ba $3d_{5/2}$ for Sn 0%, 10%, 20%, and 40% was found to be significantly higher (more positive) compared to the nonsputtered samples. Increasing the amount of Sn extracts the electron density from Ba. The Sn content is higher

at the surface; thus, this phenomenon is strong at the surface compared to the bulk. Increasing the Sn concentration replaces most of the Ba, indicating that the trend is stronger at the surface compared to the bulk. Based on the sputtering depth (~20 nm) and the surface sensitivity of XPS in the present case (~5 nm), ²³ this change of the Ba chemical state is occurring approximately over the top 20 nm of the nanoparticles used here. It needs to be noted that the sputter depth is significantly less than the previously reported thickness of the Sn outer shell. ¹⁴ Thus, the changes observed here between sputtered and nonsputtered samples are a comparison of the properties within the Sn-rich shell.

Figure 3A shows that the binding energy of Zr 3d_{5/2} for the nonsputtered sample is found at a higher binding energy range, between 182.5 and 182.7 eV, for the Sn-containing samples (10, 20, 40, and 60%), which is close to that of ZrO₂ (182.6 eV).²⁴ The binding energy of the 0% Sn sample was found at a significantly lower binding energy of 181.9 eV than that of the Sn-containing samples. While this peak is in the range of binding energies reported for ZrO₂ ranging from 182.0 to 183.3 eV,¹⁵ the lower binding energy indicates that Zr is not fully oxidized in a Zr⁴⁺ state in the 0% Sn sample.

After sputtering, the binding energy of Zr $3d_{5/2}$ is found to be close to ZrO₂ (182.6 eV) for all samples.²⁴ This means that the peak position of the Sn 10, 20, 40, and 60% samples is found at a similar binding energy compared to nonsputtered samples except for the 0% sample, which shows an increase in binding energy compared to the nonsputtered sample. The Zr concentration is rather constant across the Sn content and

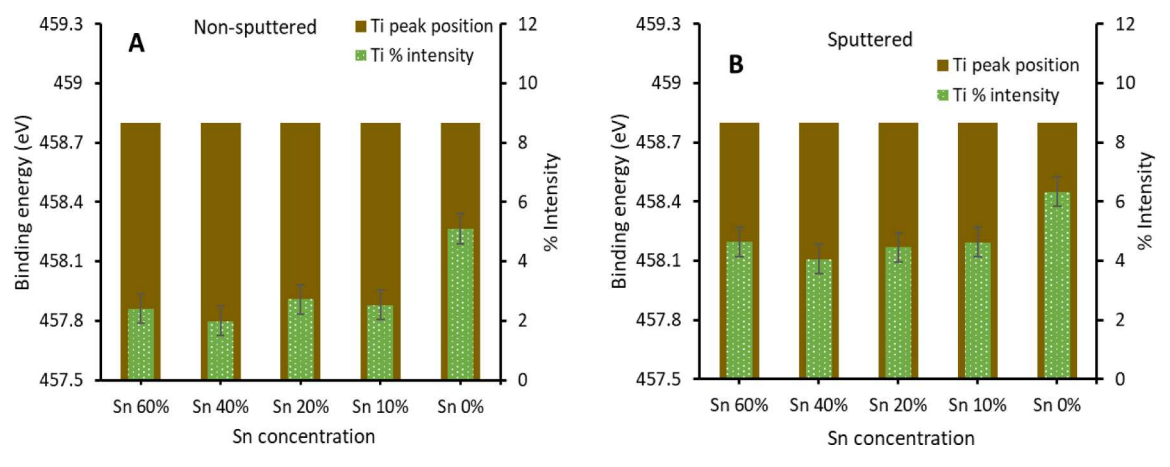


Figure 4. Plot of the binding energy vs % intensity of Ti: (A) nonsputtered and (B) sputtered.

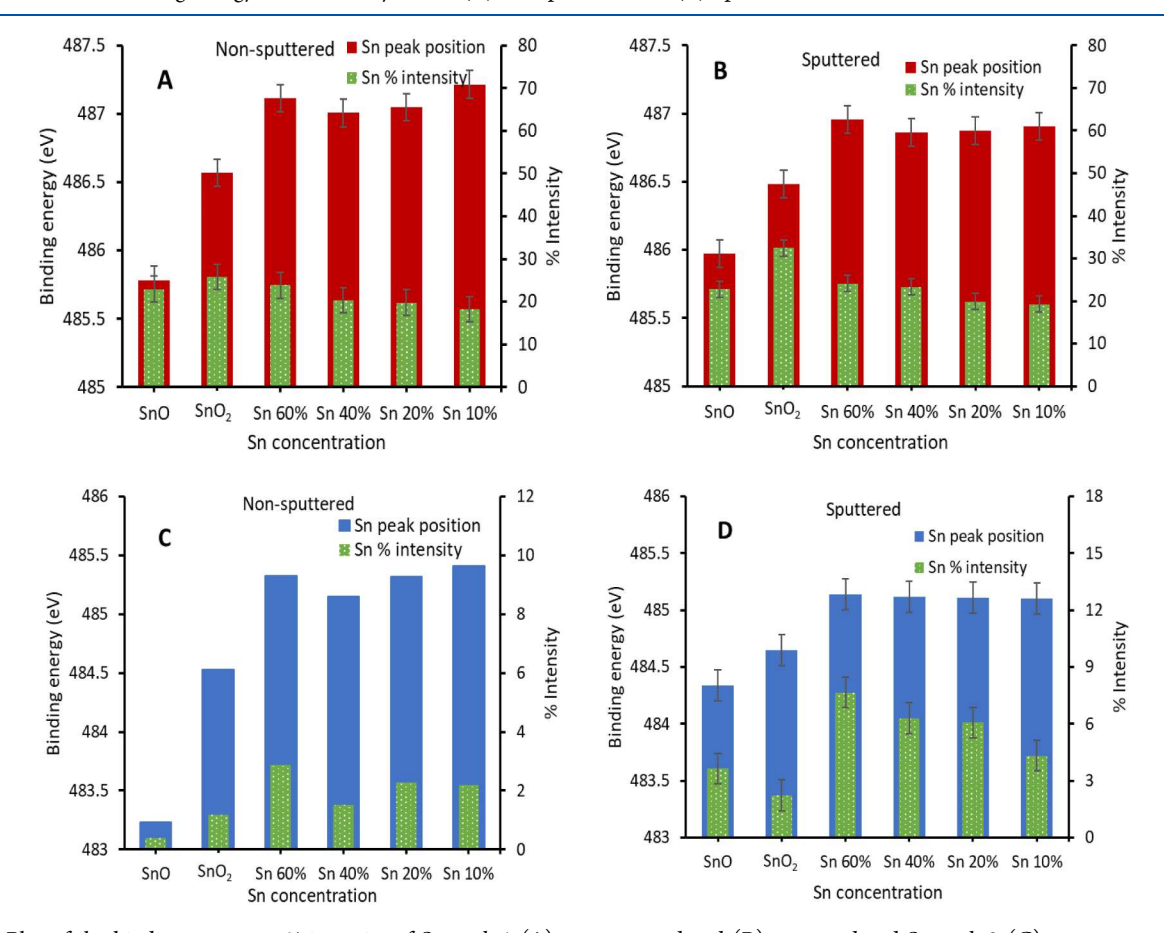


Figure 5. Plot of the binding energy vs % intensity of Sn peak 1 (A) nonsputtered and (B) sputtered and Sn peak 2 (C) nonsputtered and (D) sputtered.

increased slightly after sputtering. The Zr content and the oxidation state do not change with the Ba to Sn exchange reaction. Therefore, with reference to the probing depth as discussed above for Ba, in the outer shell of the BZT, Zr is not fully oxidized. It also can be seen that in the outer part of the shell, the Zr content decreases by about 35% from 3% relative intensity to 2%. In the inner part of the shell, there is a variation in Zr content which, however, does not seem to depend on the Sn content.

The binding energy and the intensities for Ti $2p_{3/2}$ before and after sputtering are shown in Figure 4 at the energy used for the calibration of the energy scale at 458.8 eV. The Ti

content slightly decreases upon adding Sn which is stronger in the outer shell compared to the inner part. In the outer shell, this decrease is about 50% (from 5% relative intensity to 2.5%), while in the inner part, a decrease of about 25% is observed (from 6% to 4.5% relative intensity).

The binding energies of Sn $3d_{5/2}$ are shown in Figure 5, which also includes two reference samples of SnO and SnO $_2$. The XP spectra of all six samples are provided in Figure S1 including fitting of the spectra. Sn shows two peaks (peaks 1 and 2) for all Sn samples including the SnO and SnO $_2$ reference samples. The binding energy of SnO and SnO $_2$ in the literature is found at 486.5 and 486.7 eV, respectively, 25,26

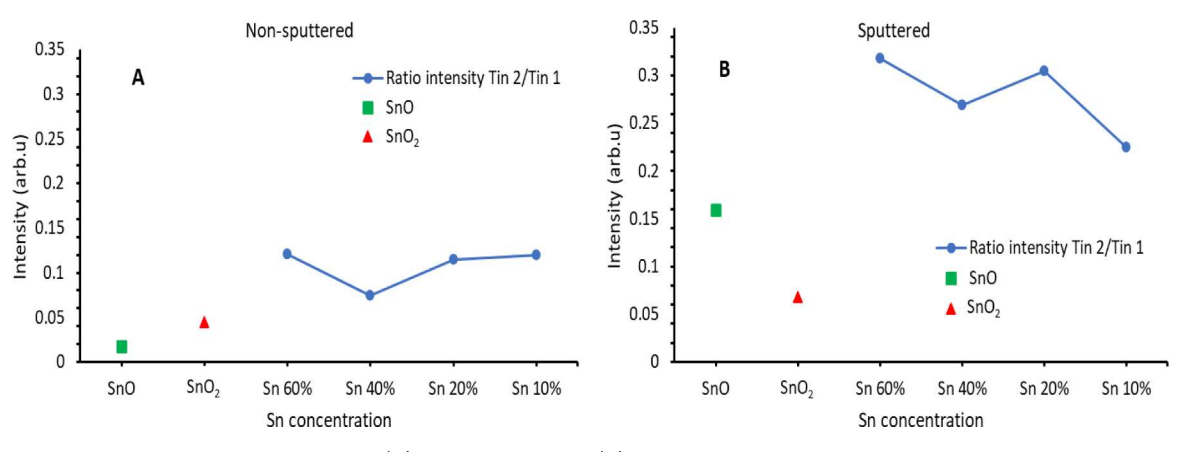


Figure 6. Ratio intensity of Sn peak 2 to peak 1 (A) nonsputtered and (B) sputtered samples.

and is almost the same within experimental uncertainty. The binding energy for metallic Sn 3d_{5/2} is reported as 484.8 eV.

From Figure 5A, the binding energy of the measured reference SnO and SnO_2 is found at 485.7 and 486.5 eV. The binding energy of Sn peak 1 for Sn 10, 20, 40, and 60% is found between 487 and 487.2 eV for Sn 10, 20, 40, and 60%, which is somewhat higher than those of both SnO and SnO_2 samples. ²⁶

For the sputtered samples, the binding energy of Sn $3d_{5/2}$ peak 1 is found between 486.8 and 486.9 eV and thus only slightly lower than that of the nonsputtered samples. It was also observed that the amount of Sn after sputtering is the same as the nonsputtered samples.

The Auger parameter of Sn was calculated for these samples to identify the oxidation state of Sn, but it was observed that the shape of the Auger line changed for some samples. It is thus unclear how to assign the Auger line reference energy in such cases. Hence, the Auger parameter could not be used to identify the oxidation state of Sn.

The binding energy of Sn $3d_{5/2}$ peak 2 is found between 485.1 and 485.4 eV for the Sn concentrations (10, 20, 40, and 60%), which formally corresponds to a lower oxidation state of Sn than for peak 1. The binding energy of Sn $3d_{5/2}$ peak 2 after sputtering is found at 485.1 eV and thus almost the same as for the nonsputtered sample. It needs to be taken into account that the binding energy of Sn has only small variations for different chemical compounds; in particular, the binding energy of SnO and SnO₂ is rather similar.²⁷ Thus, drawing conclusions about the oxidation state of Sn based on the binding energy of the $3d_{5/2}$ peak must be taken with caution.

For both peaks 1 and 2, the amount of Sn has decreased after sputtering compared to the nonsputtered samples and also increases with the nominal increase of Sn in the samples.

In Figure 6, the intensity ratio of Sn peak 2 to peak 1 is shown. The ratio is consistently higher for the BSZT samples than for the SnO and SnO₂ reference samples. For the latter SnO and SnO₂ reference samples, the second peak of SnO₂ almost does not exist. The ratio also increased with sputtering.

Changes in the XPS binding energy are usually interpreted as a change in the oxidation state. In the present case, however, it is difficult to interpret the binding energy of Sn with reference to its oxidation state. The existence of a second Sn peak in the BSZT sample could be due to the existence of two different sites in the BSZT structure and potentially in the SnO and SnO_2 sample structure as well. However, the exact nature of the two Sn peaks is not clear. The change in the intensity

ratio of the two Sn peaks could potentially be interpreted as a change in the overall oxidation state of Sn. An increase in the intensity ratio of the lower to the higher binding energy peak of Sn can then be interpreted as a decrease in the oxidation state of Sn. This interpretation would mean that Sn in the outer shell is in a somewhat higher oxidation state and would support the assumption made in a prior report. The XPS binding energies of Sn cannot be used to unambiguously identify the actual oxidation state of Sn in the samples. The Sn content increases with the nominal Sn content and lowers in the inner part of the samples with reference to the probing depth as discussed above for Ba.

The oxidation state of Sn will be further discussed in the context of NEXAFS and ¹¹⁹Sn Mössbauer spectroscopy.

Two or three peaks can be fitted to the O 1s region. The third peak at \sim 533.9 eV cannot be seen in Figure 1F. The binding energy of O 1s peak 1 is found between 530.7 and 530.8 eV for the highest Sn concentration (10, 20, 40, and 60%) which is close to the oxygen of the metal oxides (SnO₂ and ZrO₂). The binding energy of the 0% Sn samples is found at 530 eV. The relative intensity of this O peak changes only marginally with sputtering.

The binding energy of O 1s peak 1 after sputtering is found between 530.6 and 530.7 eV for all the Sn concentrations, which is very close to the O binding energies of the nonsputtered samples and thus also corresponds to the oxygen of the metal oxides $(SnO_2 \text{ and } ZrO_2)$. ^{28,29}

The binding energy of O 1s peak 2 is found between 532.4 and 532.6 eV for higher Sn concentrations (10, 20, 40, and 60%), and Sn 0% has the binding energy at 532 eV which corresponds to the binding energy of water or hydroxide.³⁰

The binding energy of O 1s peak 2 after sputtering does not change significantly, appearing between 532.2 and 532.9 eV for all the Sn concentrations. The amount of oxygen has decreased after sputtering, which is a clear sign that this is an adsorbed species on the support which is likely to be OH⁻.

Figure 7E shows a small O 1s peak 3 which is found at 533.9 eV and only for the 0% Sn sample. The peak disappears after sputtering and thus is most likely the adsorbed species such as $\rm H_2O.^{30}$

In order to provide an overview over the change of concentration of Ba, Zr, Ti, and Sn, the relative intensities of Ba, Zr, Ti, and Sn as a function of the Sn concentration for the non-sputtered and sputtered samples are shown in Figure 8. An observation becoming clearer in these figures is that the Zr and Ti contribution increases stronger in the inner part of the

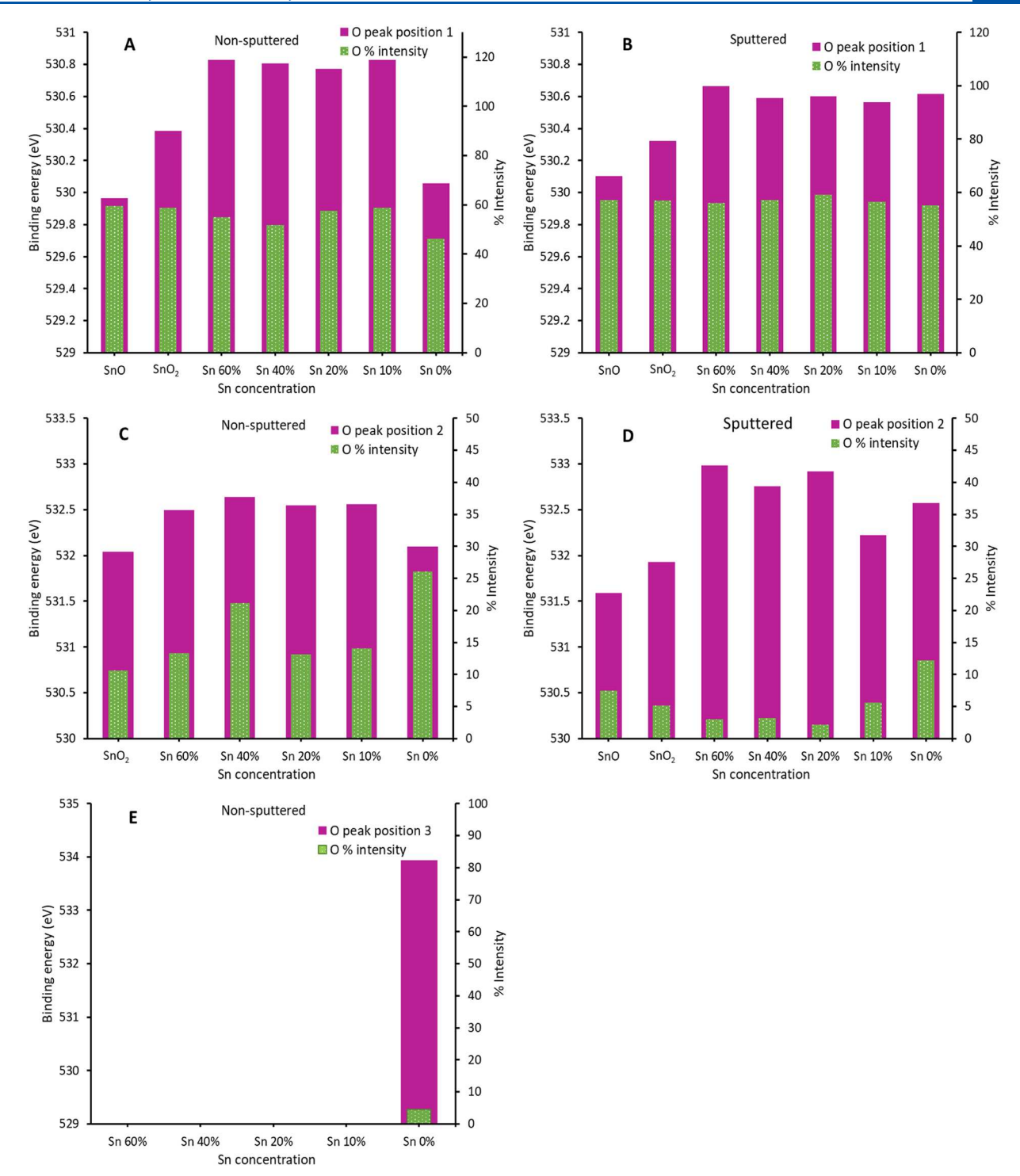


Figure 7. Plot of the binding energy vs % intensity of 1 (A) nonsputtered and (B) sputtered, O peak 2 (C) nonsputtered and (D) sputtered, and 3 (E) nonsputtered. O peak 3 has disappeared after sputtering.

sample with decreasing Sn concentration, which is due to the enriched layer of Sn in the outer shell. This is consistent with the discussion of the composition of the outer shell in the section where the oxidation state of Sn is discussed in the context of Figure 6.

NEXAFS RESULTS

In Figure 9, NEXAF spectra of both SnO and SnO₂ reference samples and of the 10% to 60% Sn-containing samples are shown. The spectra of SnO and SnO₂ are significantly different

in their characteristic features. In Figure 9A, the spectrum of SnO shows main peaks at 487.5, 492.0, 495.6, and 500.0 eV, while the reference SnO₂ sample shows peaks at 488.0, 491.0, 493.0, 495.6, 499.5, and 501.5 eV. All BSZT samples show peaks similar to SnO but are quite different to that of SnO₂. This confirms that the Sn content in the shell of the BSZT samples is mainly a Sn(II)-oxide phase and not a Sn(IV)-oxide phase.

For a more quantitative analysis, the NEXAF spectra were analyzed with the SVD algorithm. The reference spectra

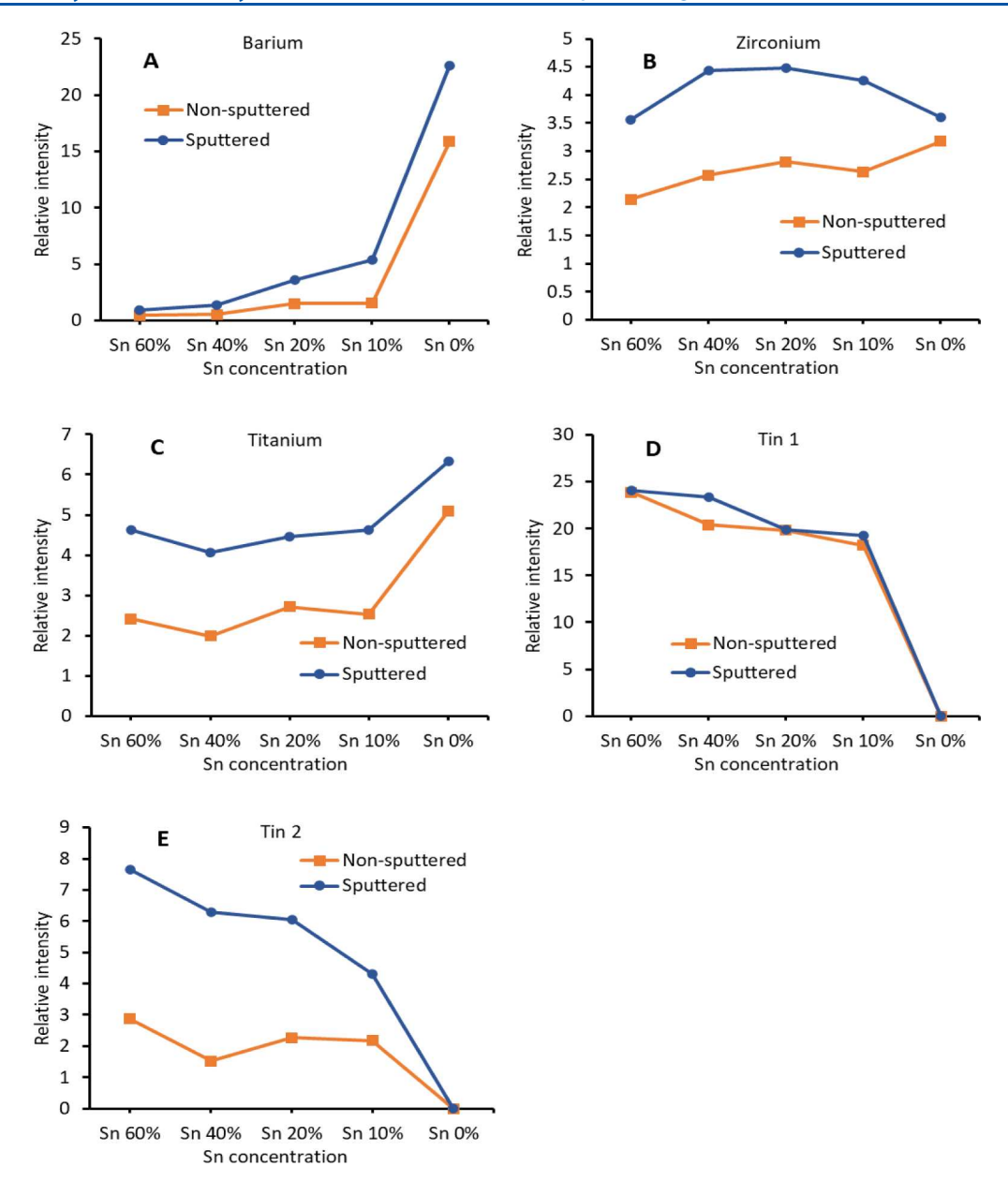


Figure 8. Relative intensity of nonsputtered and sputtered samples as a function of the Sn concentration: (A) barium, (B) zirconium, (C) titanium, (D) tin 1, and (E) tin 2.

resulting from the SVD algorithm are shown in Figure 9B, and the weighting factors are shown in Figure 9C. Reference spectra 1 and 3 have features very similar to that of the spectrum of SnO. It therefore can be concluded that both reference spectra 1 and 3 represent a Sn(II)-containing oxide. Reference spectrum 2 has features similar to those of SnO_2 shown in Figure 9A and thus corresponds to SnO_2 . This is consistent with the weighting factors from the SVD in Figure 9C. Therefore, the NEXAFS results show that the Sn-containing samples are dominant in Sn(II)-containing oxide in the outer shell probed by NEXAFS.

■ VB-XPS RESULTS

VB-XPS was performed to study the valence band cutoff in the surface region of the BSZT samples and is shown in Figure 10 where the surface region is similar but slightly larger than the probing depth of the above XPS results due to the higher kinetic energy of the electrons detected in this part of the

spectrum. However, given the experimental uncertainty of the sputtered depth, it is reasonable to assume that the nonsputtered sample probes the top 5 nm of the sample and the sputtered sample at a depth around 20 nm. The valence band edge was determined as the intersection of a straight line fitting the VB cutoff with the *x*-axis as shown in Figure 10. The region indicated in red is where the sharp drop in the VB electron density occurs. The intersection of the extrapolated linear function (fitting the cutoff) with the *x*-axis is taken as the VB cutoff. For this procedure, the dark count rate had been subtracted from the measured spectra first. As described in the Experimental section, the satellites stemming from using a nonmonochromatic X-ray source do not influence this procedure.

Figure 11A,B shows the VB cutoff of the Sn 0%, 10%, 20%, 33%, 40%, and 60% samples. The feature around 7 eV for the 0% sample relative to the Sn-containing samples is found to be increasing with the sputtered samples, and this corresponds to

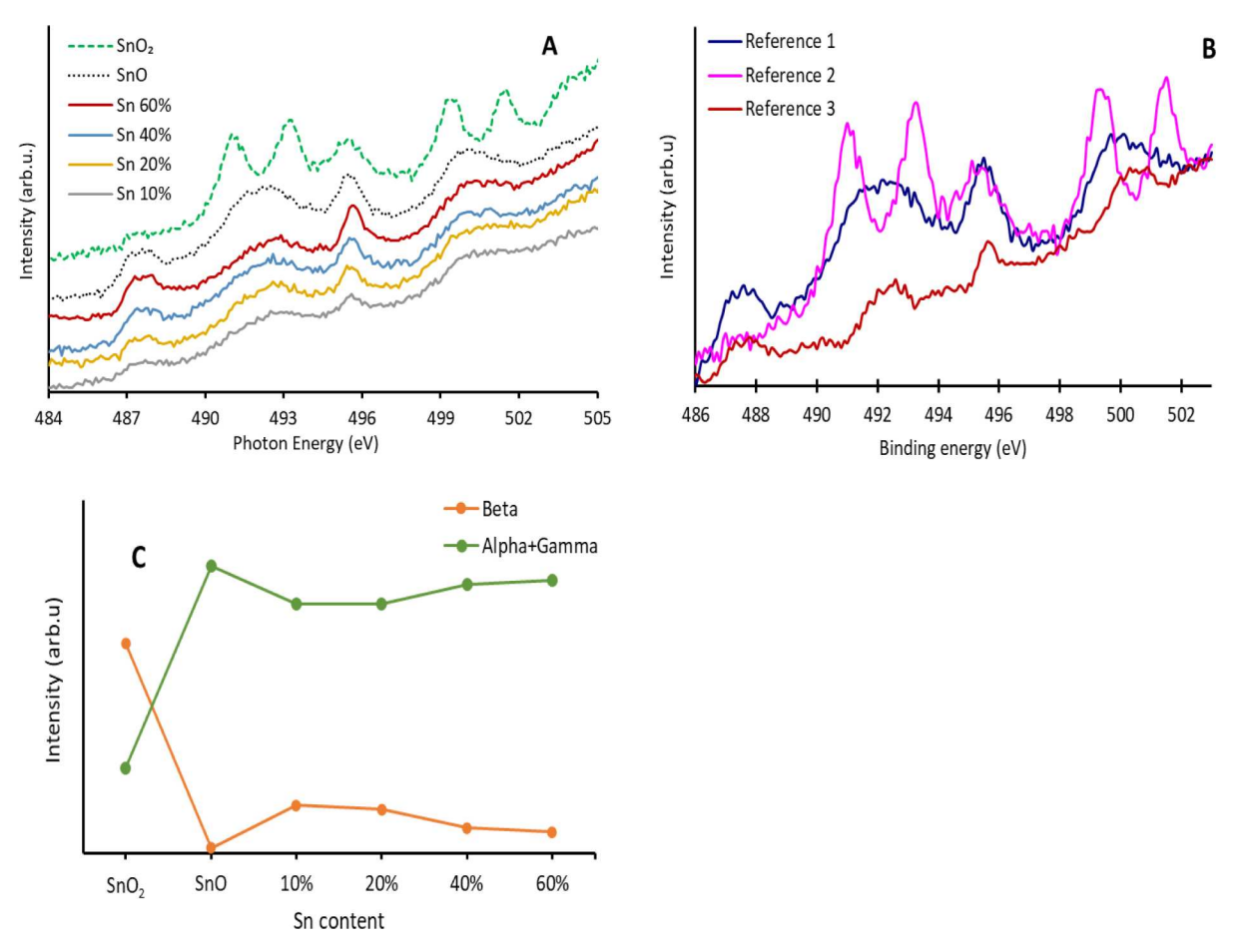


Figure 9. Plot of the comparison of the NEXAF spectra of the Sn content samples (A) with the reference SnO and SnO₂ samples, (B) NEXAFS reference spectra from the SVD algorithm, and (C) weighting factors from the SVD algorithm with alpha being the weighting factor for reference spectrum 1, beta for 2, and gamma for 3. It should be noted that reference spectra 1 and 3 are similar to the feature at 492 eV being broader for reference 1 compared to reference 3 being the main difference between the reference spectra. The fitting result would be significantly worse in case one of reference spectra 1 and 3 would be omitted or an average of the two be considered, and thus, both reference spectra are used. It is unclear which physical meaning the difference in width of the structure around 492 eV has.

the electron density at the valence electron edge due to O 2p. The reason why this region is more prominent in the Sn 0% sample is likely because the electron density of the 2p orbital has a larger energy distribution compared to the Sn-containing samples; that is, the 2p orbital is more delocalized when Sn is added to the samples.

Particularly in the sputtered sample, it can be seen that the electron density shifts to a lower binding energy with increasing Sn. In conjunction with the broadening of the O 2p feature, this likely means that the broadening of the O 2p density of states causes the lowering of the valence band cutoff, thus lowering of the band gap.

Figure 12 shows that the VB cutoff decreases with increasing Sn content. For the non-sputtered samples, the decrease is less than 1 eV, while for the sputtered samples, the decrease is almost 2 eV. Thus, Sn overall reduces the VB position. However, the decrease is much stronger for the sputtered samples and thus inside the BSZT. The decrease in the band gap measured with UV—vis is approximately the same as the decrease in the VB position as shown in our previous work. Therefore, we can assume that the CB position is not changing. Note that the conduction band could not be studied with IPES because of the particular nature of the sample (powder), leading to charging of the sample while conducting the experiment.

■ MÖSSBAUER SPECTROSCOPIC RESULTS

¹¹⁹Sn Mössbauer spectroscopy was used to study the oxidation state of Sn in the BSZT sample, and the data have been previously published in. 19 The Mössbauer spectroscopy shows that the samples contain both Sn (II) and Sn (IV) with most of the Sn (II) from the core and some Sn (IV) at the surface as was outlined in our previous work. Two samples of $(Ba_{0.8}Sn_{0.2})(Zr_{0.5}Ti_{0.5})O_3$ and $(Ba_{0.6}Sn_{0.4})(Zr_{0.5}Ti_{0.5})O_3$ showed almost similar isomer shifts of 2.98(1) and 3.02(1) mm s⁻¹ for the Sn(II) subsignals with amounts of 68% and 89% Sn(II) content, respectively. 14 While the isomer shift of the Sn(IV) contribution of 0.05 mm s⁻¹ was close to the values for SnO2, the isomer shifts of the Sn(II) subsignals are slightly higher than those of pure SnO (\sim 2.7 mm s⁻¹), indicating slightly higher electron density at the tin nuclei. 31 Also, the slightly enhanced quadrupole splitting parameters (1.86(1) and 1.83(1) mm s⁻¹ as compared to \sim 1.37 mm s⁻¹ for SnO) reflect a slightly higher asymmetry in the electron density (lone-pair character).

DISCUSSION

From the XPS results, it was found that Ba increases in binding energy with increasing Sn content. The change is stronger for non-sputtered than for sputtered samples. Thus, in the outer

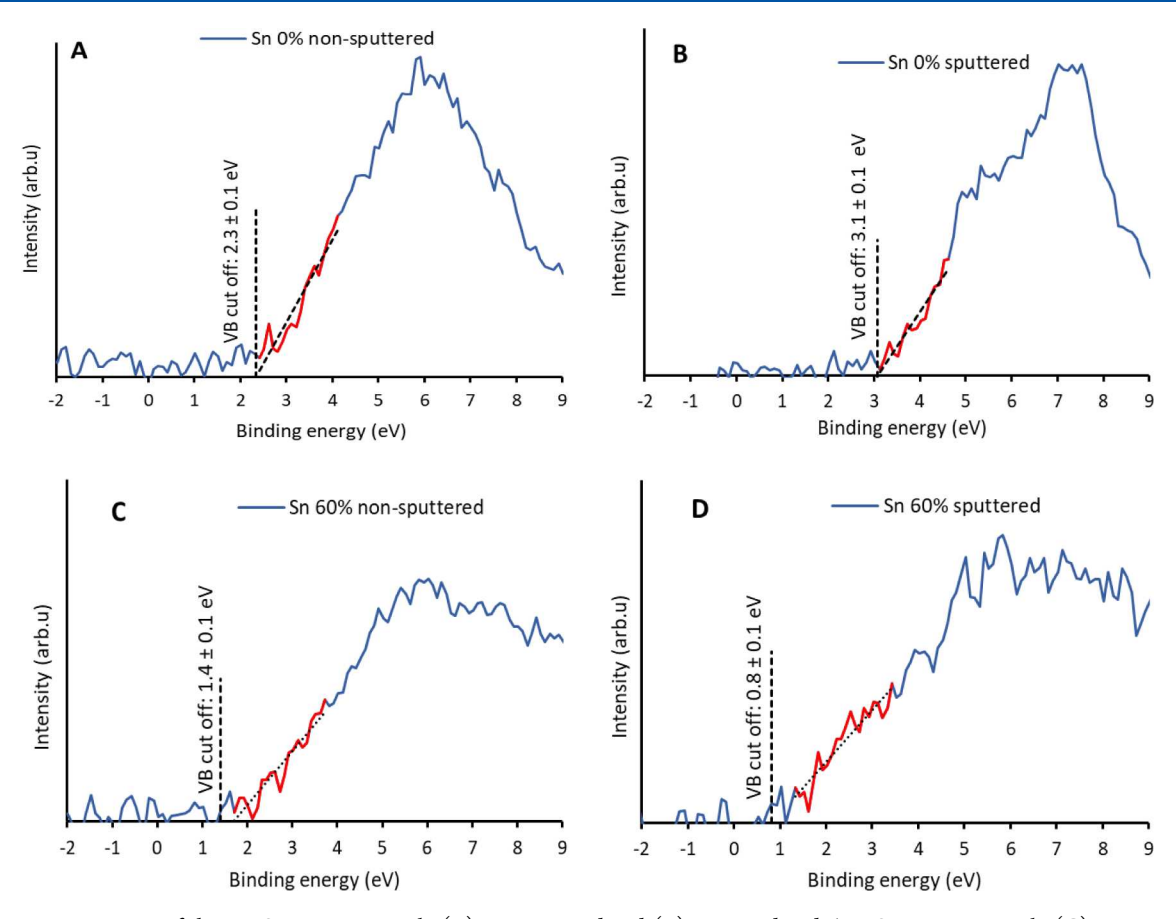


Figure 10. VB-XP spectra of the 0% Sn content sample (A) nonsputtered and (B) sputtered and 60% Sn content sample (C) nonsputtered and (D) sputtered.

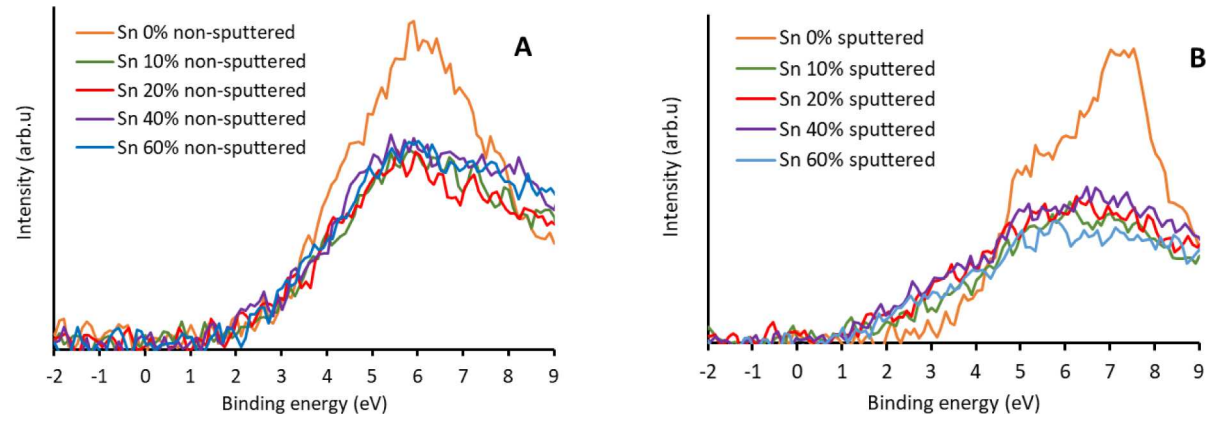


Figure 11. Comparison of the VB-XP spectra of the 0%,10%,20%, 33%, 40%, and 60% Sn content (A) nonsputtered samples and (B) sputtered samples.

part of the Sn-rich shell, the state of Sn influences Ba differently than further inside the Sn-rich shell, and the presence of Sn overall increases the oxidation state of Ba. The influence of Sn on Ba reflects that Sn and Ba form a substructure in BSZT as described previously. The Ba content increases with sputtering; thus, Sn replaces Ba mostly in the outer part of the nanoparticle in line with earlier findings. The Ba content in the 0% Sn sample is much larger than for all Sn samples which means that Sn replaces most of the Ba in the Ba/Sn substructure surface region.

Zr and Ti change with sputtering and with the Sn concentration being much less than Ba. The reason is most

likely that these two elements form a structure separate from Ba and Sn in the BSZT structure. The Ti and Zr content of the Sn samples is 10% lower than that for the 0% Sn sample. Thus, Sn also partially replaces the Ti/Zr substructure which is also seen in the XPS results (Figure 8).

Sn binding energies are similar for SnO and SnO₂, and these species are hard to distinguish. Sn shows for most samples two peaks. The dominant peak is higher in binding energy than the small peak. Both peaks are higher in binding energy than those of the SnO and SnO₂ reference samples. The binding energies of all Sn species most likely represent differences in the local environment in the BSZT structure rather than differences in

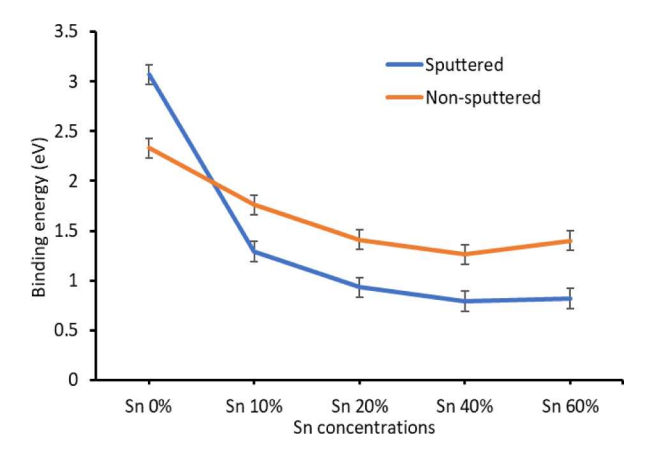


Figure 12. Plot of the comparison of VB cutoff from the VB-XP spectra of the Sn content sputtered and nonsputtered samples.

the oxidation state. The O of the metal oxide species does not change with the Sn content or with sputtering. The O of adsorbed species (H₂O and OH⁻) decreases with sputtering.

The NEXAFS and Mössbauer spectroscopy data are consistent in that Sn in the sample shell consists mainly of Sn(II)-oxide.

From the VB-XPS it was found, that the increase in the Sn content resulted in a decrease of the valence band position for both non-sputtered and sputtered samples. The decrease is stronger deeper inside the sample. The difference in the valence band position between the outer and the inner shells could be due to a slightly higher oxidation state of Sn in the outer shell or could be due to differences in the crystal structure. The change is found in the region of the O 2p electron density, and thus, the change of the VB position seems to occur mainly through the influence of change of the Sn content on the O 2p electron density such that a higher Sn concentration causes a decrease of the VB cutoff.

Overall, the findings show that the flux reaction adding Sn to the samples replaces mainly Ba in the Ba/Sn substructure of the BSZT and also in the Ti/Zr substructure but only to a small degree. Ba in the outer part of the sample is in a lower oxidation state than that in the inner part. In the case that only a small amount of Sn is present at a specific location, a lower oxidation state of Ba is promoted. The increase in Sn content leads to a decrease of the VB cutoff energy; however, this effect is stronger in the inner part of the sample and coincides with an increase in the binding energy of Ba. The decrease in the VB cutoff in the outer shell also coincides with an increase in the binding energy of Zr.

CONCLUSION

The chemical structure and the state of Sn in the metastable oxide BSZT were studied using XPS, NEXAFS, and ¹¹⁹Sn Mössbauer spectroscopy. The results revealed that the oxidation state of Sn does not change with Sn concentration. However, the chemical environment of Sn changes from the surface to the bulk. It is also revealed that the chemical state of Sn corresponds mainly to oxidic SnO in the divalent state with a potential tendency to be in a higher oxidation state in the outer shell. A valence band gradient is caused by the flux reaction of Sn in the core—shell structure. The increase in Sn content decreases the VB position, which occurs to a stronger degree in the inner part of the BSZT. The influence of Sn seems to be mainly on the electron density related to the 2p

electrons. The decrease in the VB position is the same as the change in the band gap overall as measured with UV—vis; thus, the CB position probably does not change. Due to the gradient, there is a driving force to get the holes to the surface, but the electrons are not affected. Hence, these metastable perovskite oxides are not suitable for overall photocatalytic water splitting but may be used for the water oxidation half reaction.

ASSOCIATED CONTENT

Supporting Information

The Supporting Information is available free of charge at https://pubs.acs.org/doi/10.1021/acs.jpcc.4c04169.

XP spectra of all six samples covering the range of Sn content investigated including fitting of the spectra (PDF)

AUTHOR INFORMATION

Corresponding Author

Gunther G. Andersson — Flinders Institute for Nanoscale Science and Technology, Flinders University, Adelaide, South Australia 5001, Australia; oorcid.org/0000-0001-5742-3037; Email: gunther.andersson@flinders.edu.au

Authors

Gowri Krishnan – Flinders Institute for Nanoscale Science and Technology, Flinders University, Adelaide, South Australia 5001, Australia

Shaun O'Donnell – Department of Chemistry, North Carolina State University, Raleigh, North Carolina 27695-8204, United States; orcid.org/0000-0003-1487-4836

Rachel Broughton – Department of Chemistry, North Carolina State University, Raleigh, North Carolina 27695-8204, United States

Jacob L. Jones – Department of Chemistry, North Carolina State University, Raleigh, North Carolina 27695-8204, United States; © orcid.org/0000-0002-9182-0957

D. J. Osborn – Department of Chemistry, The University of Adelaide, Adelaide, South Australia 5005, Australia

Thomas D. Small – Department of Chemistry, The University of Adelaide, Adelaide, South Australia 5005, Australia

Theresa Block – Institut für Anorganische und Analytische Chemie, Universität Münster, Münster 48149, Germany

Aylin Koldemir – Institut für Anorganische und Analytische Chemie, Universität Münster, Münster 48149, Germany

Rainer Pöttgen – Institut für Anorganische und Analytische Chemie, Universität Münster, Münster 48149, Germany

Gregory F. Metha — Department of Chemistry, The University of Adelaide, Adelaide, South Australia 5005, Australia; orcid.org/0000-0003-1094-0947

Paul A. Maggard — Department of Chemistry, North Carolina State University, Raleigh, North Carolina 27695-8204, United States; orcid.org/0000-0002-3909-1590

Complete contact information is available at: https://pubs.acs.org/10.1021/acs.jpcc.4c04169

Notes

The authors declare no competing financial interest.

ACKNOWLEDGMENTS

The authors acknowledge the Australian National Fabrication Facility (ANFF) and Microscopy Australia (formerly known as

the Australian Microscopy and Microanalysis Research Facility (AMMRF)) for their facilities and scientific and technical support. The authors acknowledge Flinders Microscopy and Microanalysis and their expertise. P.M. acknowledges partial support of this work by the National Science Foundation (DMR-2004455).

REFERENCES

- (1) Lopez, N.; Janssens, T.; Clausen, B.; Xu, Y.; Mavrikakis, M.; Bligaard, T.; Nørskov, J. K. On the origin of the catalytic activity of gold nanoparticles for low-temperature CO oxidation. *J. Catal.* **2004**, 223, 232–235.
- (2) Valden, M.; Lai, X.; Goodman, D. W. Onset of Catalytic Activity of Gold Clusters on Titania with the Appearance of Nonmetallic Properties. *Science* **1998**, *281*, 1647–1650.
- (3) Choudhary, T.; Goodman, D. Catalytically active gold: The role of cluster morphology. *Appl. Catal., A* **2005**, 291, 32–36.
- (4) Wang, Q.; Domen, K. Particulate photocatalysts for light-driven water splitting: Mechanisms, challenges, and design strategies. *Chem. Rev.* **2020**, *120*, 919–985.
- (5) Fujishima, A.; Honda, K. Electrochemical Photolysis of Water at a Semiconductor Electrode. *Nature* **1972**, 238, 37–38.
- (6) Pattanayak, P.; Singh, P.; Bansal, N. K.; Paul, M.; Dixit, H.; Porwal, S.; Mishra, S.; Singh, T. Recent progress in perovskite transition metal oxide-based photocatalyst and photoelectrode materials for solar-driven water splitting. *J. Environ. Chem. Eng.* **2022**, *10*, 108429.
- (7) Shi, R.; Waterhouse, G. I. N.; Zhang, T. Recent progress in photocatalytic CO2 reduction over perovskite oxides. *Sol. RRL* **2017**, 1, 1700126.
- (8) Zhang, H.; Ji, X.; Xu, H.; Zhang, R.; Zhang, H. Design and Modification of Perovskite Materials for Photocatalysis Performance Improvement. *J. Environ. Chem. Eng.* **2023**, *11*, 109056.
- (9) Miyauchi, M.; Nakajima, A.; Fujishima, A.; Hashimoto, K.; Watanabe, T. Photoinduced surface reactions on TiO2 and SrTiO3 films: photocatalytic oxidation and photoinduced hydrophilicity. *Chem. Mater.* **2000**, *12*, 3–5.
- (10) Fu, Q.; Wagner, T. Metal/oxide interfacial reactions: Oxidation of metals on SrTiO3 (100) and TiO2 (110). *J. Phys. Chem. B* **2005**, 109, 11697–11705.
- (11) Konta, R.; Ishii, T.; Kato, H.; Kudo, A. Photocatalytic Activities of Noble Metal Ion Doped SrTiO3 under Visible Light Irradiation. *J. Phys. Chem. B* **2004**, *108*, 8992–8995.
- (12) Miseki, Y.; Kato, H.; Kudo, A. Water splitting into H 2 and O 2 over niobate and titanate photocatalysts with (111) plane-type layered perovskite structure. *Energy Environ. Sci.* **2009**, *2*, 306–314.
- (13) O'Donnell, S.; Chung, C.-C.; Carbone, A.; Broughton, R.; Jones, J. L.; Maggard, P. A. Pushing the Limits of Metastability in Semiconducting Perovskite Oxides for Visible-Light-Driven Water Oxidation. *Chem. Mater.* **2020**, *32*, 3054–3064.
- (14) O'Donnell, S.; Osborn, D. J.; Krishnan, G.; Block, T.; Koldemir, A.; Small, T. D.; Broughton, R.; Jones, J. L.; Pöttgen, R.; Andersson, G. G.; Metha, G. F.; Maggard, P. A. Prediction and Kinetic Stabilization of Sn(II)-Perovskite Oxide Nanoshells. *Chem. Mater.* **2022**, *34*, 8054–8064.
- (15) Naumkin, A. V.; Kraut-Vass, A.; Gaarenstroom, S. W.; Powell, C. J. NIST X-ray Photoelectron Spectroscopy Database, Version 4.1, National Institute of Standards and Technology: Gaithersburg. 2012.
- (16) Hahner, G. Near Edge X-ray Absorption Fine Structure Spectroscopy as a Tool to Probe Electronic and Structural Properties of Thin Organic Films and Liquids. *Chem. Soc. Rev.* **2006**, *35*, 1244–1255.
- (17) Long, G. J.; Cranshaw, T.; Longworth, G. The ideal Mössbauer effect absorber thickness. Möss. Eff. Ref. Data J. 1983, 6, 42–49.
- (18) Brand, R. WinNormos for Igoró (version for Igor 6.2 or above: 22/02/2017). Universität Duisburg: Duisburg, Germany, 2017.
- (19) O'Donnell, S.; Osborn, D. J.; Krishnan, G.; Block, T.; Koldemir, A.; Small, T. D.; Broughton, R.; Jones, J. L.; Pöttgen, R.; Andersson,

- G. G.; et al. Prediction and Kinetic Stabilization of Sn (II)-Perovskite Oxide Nanoshells. *Chem. Mater.* **2022**, *34*, 8054–8064.
- (20) Hofmann, S. Sputter depth profiling: Past, present, and future. Surf. Interface Anal. 2014, 46, 654–662.
- (21) Vasquez, R. X-ray photoelectron spectroscopy study of Sr and Ba compounds. J. Electron Spectrosc. Relat. Phenom. 1991, 56, 217–240.
- (22) Gauzzi, A.; Mathieu, H. J.; James, J. H.; Kellett, B. AES, XPS and SIMS characterization of YBa2Cu3O7 superconducting high Tc thin films. *Vacuum* **1990**, *41*, 870–874.
- (23) Tanuma, S.; Powell, C. J.; Penn, D. R. Calculations of electron inelastic mean free paths. *Surf. Interface Anal.* **2005**, *37*, 1–14.
- (24) Morant, C.; Sanz, J.; Galan, L.; Soriano, L.; Rueda, F. An XPS study of the interaction of oxygen with zirconium. *Surf. Sci.* **1989**, *218*, 331–345.
- (25) Grutsch, P.; Zeller, M.; Fehlner, T. Photoelectron spectroscopy of tin compounds. *Inorg. Chem.* **1973**, *12*, 1431–1433.
- (26) Chuvenkova, O. A.; Domashevskaya, E. P.; Ryabtsev, S. V.; Yurakov, Y. A.; Popov, A. E.; Koyuda, D. A.; Nesterov, D. N.; Spirin, D. E.; Ovsyannikov, R. Y.; Turishchev, S. Y. XANES and XPS investigations of surface defects in wire-like SnO2 crystals. *Phys. Solid State* **2015**, *57*, 153–161.
- (27) Moulder, J. F.; Stickle, W. F.; Sobol, P. E.; Bomben, K. D. *Handbook of X-ray Photoelectron Spectroscopy*; Physical Electronics, Inc.: Eden Prairie, 1995.
- (28) Lin, A. W.; Armstrong, N. R.; Kuwana, T. X-ray photoelectron/ Auger electron spectroscopic studies of tin and indium metal foils and oxides. *Anal. Chem.* **1977**, *49*, 1228–1235.
- (29) Moses, P.; Wier, L. M.; Lennox, J. C.; Finklea, H.; Lenhard, J.; Murray, R. W. X-ray photoelectron spectroscopy of alkylaminesilanes bound to metal oxide electrodes. *Anal. Chem.* **1978**, *50*, *576*–*585*.
- (30) Martensson, N.; Malmqvist, P.-A.; Svensson, S.; Basilier, E.; Pireaux, J.-J.; Gelius, U.; Siegbahn, K. Molecular and solid water-A comparative ESCA study. *Nouv. J. Chim.* **1977**, *1*, 191–196.
- (31) Lippens, P. Interpretation of the 119 Sn Mössbauer isomer shifts in complex tin chalcogenides. *Phys. Rev. B* **1999**, *60*, 4576.